

## Article

# Molten-Salt-Assisted Synthesis of Nitrogen-Doped Carbon Nanosheets Derived from Biomass Waste of Gingko Shells as Efficient Catalyst for Oxygen Reduction Reaction

Wei Hong <sup>1,†</sup>, Xia Wang <sup>1,†</sup>, Hongying Zheng <sup>1</sup>, Rong Li <sup>1,\*</sup>, Rui Wu <sup>2,\*</sup> and Jun Song Chen <sup>2,\*</sup> 

<sup>1</sup> Chemical Synthesis and Pollution Control Key Laboratory of Sichuan Province, College of Chemistry and Chemical Engineering, China West Normal University, Nanchong 637000, China; hongweicqu@163.com (W.H.); luwckxy@163.com (X.W.); 18380585773@163.com (H.Z.)

<sup>2</sup> School of Materials and Energy, University of Electronic Science and Technology of China, Chengdu 611731, China

\* Correspondence: lirong406b@126.com (R.L.); ruiwu0904@uestc.edu.cn (R.W.); jschen@uestc.edu.cn (J.S.C.)

† These authors contributed equally to this work.

**Abstract:** Developing superior efficient and durable oxygen reduction reaction (ORR) catalysts is critical for high-performance fuel cells and metal–air batteries. Herein, we successfully prepared a 3D, high-level nitrogen-doped, metal-free (N–pC) electrocatalyst employing urea as a single nitrogen source, NaCl as a fully sealed nanoreactor and gingko shells, a biomass waste, as carbon precursor. Due to the high content of active nitrogen groups, large surface area ( $1133.8 \text{ m}^2 \text{ g}^{-1}$ ), and 3D hierarchical porous network structure, the as-prepared N–pC has better ORR electrocatalytic performance than the commercial Pt/C and most metal-free carbon materials in alkaline media. Additionally, when N–pC was used as a catalyst for an air electrode, the Zn–air battery (ZAB) had higher peak power density ( $223 \text{ mW cm}^{-2}$ ), larger specific-capacity ( $755 \text{ mAh g}^{-1}$ ) and better rate-capability than the commercial Pt/C-based one, displaying a good application prospect in metal–air batteries.

**Keywords:** N-doped carbon nanosheet; gingko shells; oxygen reduction reaction; Zn–air battery



**Citation:** Hong, W.; Wang, X.; Zheng, H.; Li, R.; Wu, R.; Chen, J.S. Molten-Salt-Assisted Synthesis of Nitrogen-Doped Carbon Nanosheets Derived from Biomass Waste of Gingko Shells as Efficient Catalyst for Oxygen Reduction Reaction. *Processes* **2021**, *9*, 2124. <https://doi.org/10.3390/pr9122124>

Academic Editors: Sergey Zhironkin and Radim Rybar

Received: 14 October 2021

Accepted: 22 November 2021

Published: 25 November 2021

**Publisher's Note:** MDPI stays neutral with regard to jurisdictional claims in published maps and institutional affiliations.



**Copyright:** © 2021 by the authors. Licensee MDPI, Basel, Switzerland. This article is an open access article distributed under the terms and conditions of the Creative Commons Attribution (CC BY) license (<https://creativecommons.org/licenses/by/4.0/>).

## 1. Introduction

The oxygen reduction reaction (ORR) plays a key role in fuel cells and metal–air batteries to implement electrochemical energy conversion [1,2]. However, the sluggishness of ORR kinetics at the cathode limits their commercial application [3,4]. Pt and its alloys materials, recognized as the best ORR electrocatalysts, suffer from the resource deficiency, prohibitive cost and inferior durability [5,6]. Consequently, development of earth-abundance, cost-effective and performance-stable catalysts to substitute the precious-based catalysts for ORR is crucial yet challenging [7–9].

Heteroatom-doped carbon materials, such as P-doped carbon xerogel [10], N-doped nanotube [11,12], S-doped carbon [13,14] and B-doped graphene [15], are among the most promising electrocatalysts for ORR due to their advantages of relatively low cost, abundant reserves, good electronic conductivity and environmental friendliness [16,17]. Among them, N-doping has been considered to be one of the most effectual ways to enhance the electrocatalytic activities of carbon materials for ORR [18,19] because the N-doping can improve the electrical conductivity of carbon and change the charge distribution of the carbon atoms close to the dopants and then make them positively charged, which is beneficial to the adsorption and reduction of oxygen at the corresponding sites and improving the ORR activity [7,20,21].

However, the morphology of N-doped carbon materials prepared by traditional methods is hardly controlled, and the content of the N-dopant is relatively low because of the volatilization of the N element at high temperature, which has an undesirable effect on

the electrocatalytic performance of the prepared materials. The employment of nanoreactor during the synthesis process can help relieve these challenges. The assistance of inorganic salts, such as NaCl [22,23], MgO [24], SiO<sub>2</sub> [25,26] and Fe<sub>3</sub>O<sub>4</sub> [27], has been considered to be an effective strategy to prepare porous carbon materials. Among them, NaCl is one of the most commonly used because NaCl can not only act as a confining agent to reduce the weight loss of precursors and promote the N-doping during the high-temperature pyrolysis process but also as pore-forming agents to promote the production of macro-pores and a 3D network structure. In addition, NaCl can be conveniently removed by water-washing with no use of any corrosive and harmful chemicals and can be facilely recycled by recrystallization. However, a cost-effective and large-scale synthetic production method is still highly desirable but challenging. During the past decade, various biomass-derived carbon ORR catalysts have aroused ever-growing attention [28–31]. Gingko is mainly used for food and medicine, but the shells are usually thrown away as garbage, which not only causes a huge waste of resources but also leads to environmental pollution.

Herein, we report a molten-salt-assisted strategy to fabricate a 3D high-level nitrogen-doped porous carbon nanosheets network (N–pC) by a facile high-temperature pyrolysis method, employing the carbon-enriched biomass waste of gingko shells and urea as a carbon precursor and NaCl and urea as a fully sealed nanoreactor and a nitrogen source, respectively. The merits, such as large specific surface area, hierarchical pore structure and high active nitrogen (pyridinic and graphitic-N) content, endow the obtained N–pC excellent electrocatalytic ORR performance in alkaline solution, much superior to commercial Pt/C and most of the reported N-doped carbon materials. Inspired by the excellent ORR catalytic performance, the prepared N–pC was further used to assemble Zn-air batteries, which showed high peak power density, large specific-capacity and good rate-capability, making it a competitive alternative to the application in metal-air batteries.

## 2. Materials and Methods

### 2.1. Synthesis of the Materials

N–pC was prepared by pyrolyzing the mixture of gingko shells, NaCl and urea. Typically, 0.5 g gingko shells rinsed by deionized water, 1.4 g NaCl and 4 g urea were mixed to refined powder by planetary ball-milling for 4 h. Then, the mixture was initially carbonized under Ar atmosphere at 750 °C for 2 h with a ramp rate of 3 °C min<sup>-1</sup>. Subsequently, the obtained product was refluxed in 3 M HCl (50 mL) for 6 h and washed with deionized water 3 times. After being dried at 80 °C for 24 h, the obtained black powder was further pyrolyzed at 900 °C for 2 h, and then the final product (N–pC) was harvested. For comparison, N–C catalyst was fabricated through the same procedure in the absence of NaCl. C catalyst was also synthesized by direct pyrolysis of the gingko shell powder.

### 2.2. Characterizations

Rigaku Ultima IV diffractometer (Cu K $\alpha$  radiation) was employed to obtain the X-ray diffraction (XRD) spectra. Microstructural morphologies were observed employing field emission scanning electron microscopy (SEM, ZEISS SUPRA 55) and transmission electron microscope (TEM, JEM-2100F). To analyze the specific surface areas and pore-size distribution, nitrogen adsorption–desorption isotherms were tested on ASAP 2000 analyzer. X-ray photoelectron spectroscopy (XPS) measurement was implemented employing a Thermo Scientific Escalab 250 Xi.

### 2.3. Electrochemical Measurements

All the electrochemical tests were implemented on bipotentiostat (CHI760E, Shanghai, China) assembled with a rotation system (Pine Research Instrumentation, Durham, NC, USA) in a three-electrode system. A carbon rod, an Ag/AgCl electrode (in saturated KCl solution) and a glassy carbon electrode (GCE) loaded with various catalyst (N–pC, N–C, C or benchmark 20 wt.% Pt/C) were used as the counter electrode, reference electrode, and working electrode, respectively. To prepare the working electrode, 14  $\mu$ L the catalyst ink

obtained by dispersing 1 mg catalyst powder into 0.5 mL Nafion solution (0.05 wt.%) via sonication was dropped onto the GCE, keeping the catalyst loading of  $141.6 \mu\text{g cm}^{-2}$ . All potentials versus Ag/AgCl electrode ( $E_{\text{Ag}/\text{AgCl}}$ ) were converted to the reversible hydrogen electrode ( $E_{\text{RHE}}$ ) based on the formula of  $E_{\text{RHE}} = E_{\text{Ag}/\text{AgCl}} + E^{\theta}_{\text{Ag}/\text{AgCl}} + 0.059\text{pH}$ .

Cyclic voltammetry (CV) and linear sweep voltammetry (LSV) measurements were carried out in 0.1 M KOH electrolyte at a scanning rate of  $100 \text{ mV s}^{-1}$  and  $10 \text{ mV s}^{-1}$ , respectively. The electron transfer number ( $n$ ) was calculated using the Koutecky–Levich (K-L) equation:

$$\frac{1}{J} = \frac{1}{J_k} + \frac{1}{B\omega^{1/2}} \quad (1)$$

$$B = 0.62nFC_0D_0^{2/3}v^{1/6} \quad (2)$$

where  $J$  and  $J_k$  are the measured disk's current density and the kinetic current density, respectively,  $\omega$  is the angular velocity of rotation.  $F$  is the Faraday constant ( $96,485 \text{ C mol}^{-1}$ ),  $C_0$  is the  $\text{O}_2$  concentration in electrolyte ( $1.2 \times 10^{-6} \text{ mol cm}^{-3}$ ),  $D_0$  is the  $\text{O}_2$  diffusion coefficient ( $1.9 \times 10^{-5} \text{ cm}^2 \text{ s}^{-1}$ ), and  $v$  represents the kinematic viscosity of the electrolyte ( $1.13 \times 10^{-2} \text{ cm}^2 \text{ s}^{-1}$ ).

The yield of  $\text{HO}_2^-$  and the  $n$  values for ORR via the RRDE measurements were determined by the equations as below:

$$\text{HO}_2^- \% = 200 \times \frac{I_r/N}{I_d + I_r/N} \quad (3)$$

$$n = 4 \times \frac{I_d}{I_d + I_r/N} \quad (4)$$

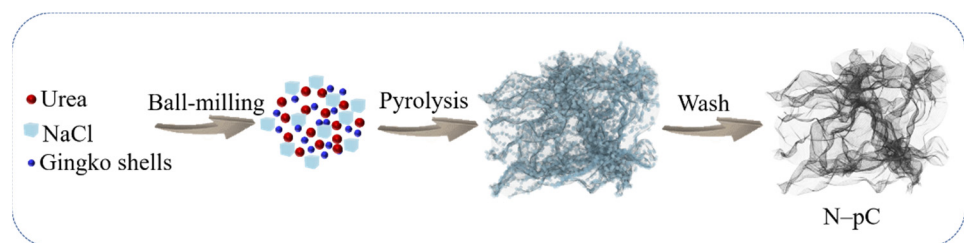
where  $I_d$  and  $I_r$  are the current density on disk and ring electrode, respectively, and  $N$  is the current collection efficiency of Pt ring, which is equal to 0.37.

The durability and the possible methanol crossover effect of N–pC and benchmark Pt/C catalyst were evaluated by chronoamperometric measurement at a rotation of 1600 rpm and a fixed potential of 0.7 V (versus RHE) in the  $\text{O}_2$ -saturated 0.1 M KOH solution.

The homemade Zn–air battery (ZAB) was equipped with a polished pure Zn plate (0.5 mm in thickness) as the anode, carbon paper ( $2 \text{ cm} \times 2 \text{ cm}$ ) uniformly coated with the catalyst (N–pC or benchmark 20 wt.% Pt/C, mass loading:  $1 \text{ mg cm}^{-2}$ ) as the air cathode and 6 M KOH solution as the electrolyte.

### 3. Results and Discussion

The synthetic procedures of N–pC are illustrated in Scheme 1. Gingko shells, NaCl and urea were first mixed to a refined powder by ball-milling. Then, the powder was initially carbonized at  $750^\circ\text{C}$  (slightly lower than the melting point of NaCl to avoid the structural collapse of newly formed carbon materials). After the removal of NaCl by water washing and further pyrolysis at  $900^\circ\text{C}$  to increase the graphitization degree and conductivity, the final product (N–pC) was obtained. The compositions of the C, N–C and N–pC were characterized by XRD. As shown in Figure 1, the diffraction peaks of C, N–C and N–pC at  $26^\circ$  and  $44^\circ$  correspond to the (002) and (101) planes of graphite carbon, respectively, indicating that gingko shells have been successfully transformed into carbon materials under high-temperature pyrolysis. The characteristic peaks of NaCl cannot be observed in N–pC, indicating that the NaCl template can be removed by simple washing. In addition, we notice that the peak intensity weakens in the order of C, N–C and N–pC, suggesting that N-doping can increase the number of defect sites and the addition of NaCl can further induce the formation of more defect sites.



**Scheme 1.** Schematic illustration of the preparation of the N-pC catalyst.

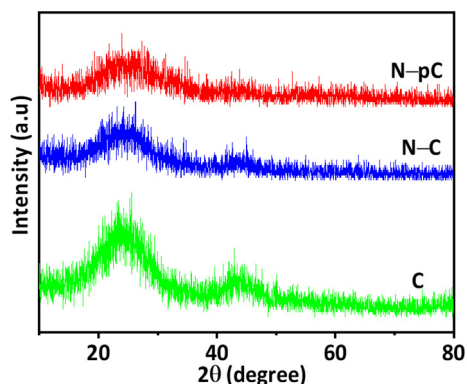


**Figure 1.** XRD patterns of C, N-C and N-pC.

The morphologies of the synthesized materials were observed by SEM and TEM. As shown in Figure 2a, the C catalyst obtained from the direct pyrolysis of gingko shells without the addition of urea and NaCl presents a compact and irregular block, whereas N-C has a significantly much looser and more porous morphology (Figure 2b), which mostly results from the large amount of pyrolysis gas of urea. With the further addition of NaCl, acted as sealed nanoreactor, the N-pC shows a 3D porous networks structure composed of graphene-like nanosheets (Figure 2c), which is beneficial to the increase of the specific surface area, the exposure of more active sites, and the improvement of transport rate of various substances involved in the reaction. TEM results are consistent with SEM. As shown in Figure 2d,e, the N-pC consists of a large number of graphene-like thin nanosheets, which interleave with each other, resulting in the formation of hierarchical pore structure and somewhat distorted of the carbon crystal faces. According to the elemental mapping (Figure 2f), the elements C, N and O are homogeneously distributed in the nanosheet, indicating the successful doping of N in N-pC catalyst.

The effect of urea and NaCl was further investigated by nitrogen adsorption/desorption measurements. As shown in Figure 3a, a distinct nitrogen uptake occurs at relative low pressure and a hysteresis loop appears at medium pressure in the isotherm curves of C, N-C and N-pC, indicating the existence of micro- and meso-pores in the three samples, which may be ascribed to the gas released from the decomposition of urea and gingko shells in the carbonization process. In addition, the isothermal adsorption curve of N-pC shows a sharp adsorption in the relative high-pressure region, demonstrating the existence of macropores on the material as the result of the occupying space of NaCl. The corresponding pore size distribution of the three materials (Figure 3b) further confirms their porous structures. Due to the different pore structure, the specific surface area and pore volume of C ( $641.9 \text{ m}^2 \text{ g}^{-1}$ ,  $0.365 \text{ cm}^3 \text{ g}^{-1}$ ), N-C ( $1102.6 \text{ m}^2 \text{ g}^{-1}$ ,  $1.026 \text{ cm}^3 \text{ g}^{-1}$ ) and N-pC ( $1133.8 \text{ m}^2 \text{ g}^{-1}$ ,  $1.22 \text{ cm}^3 \text{ g}^{-1}$ ) are different. The large specific surface area and pore volume of N-pC means it can fully expose the active sites and most effectively accelerate mass transport, thus improving the electrochemical catalytic performance.

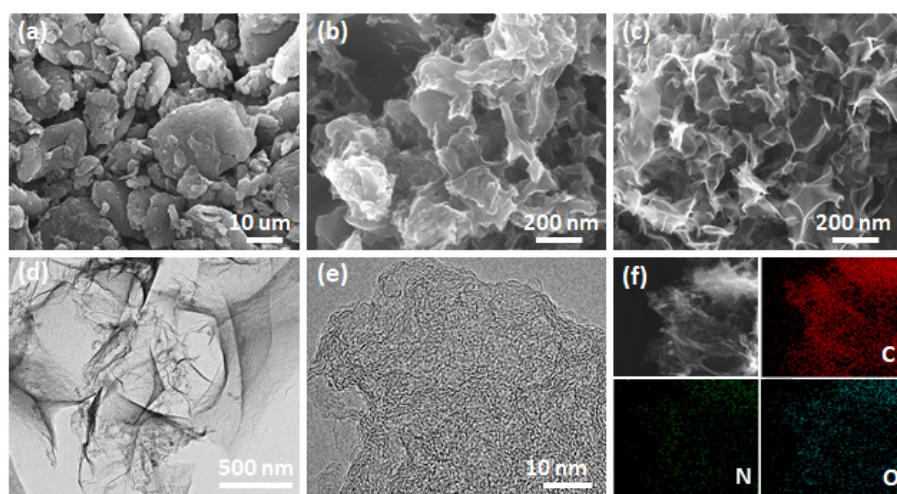


**Figure 2.** SEM images of (a) C, (b) N-C and (c) N-pC; (d) TEM; (e) HRTEM; and (f) element mapping images of N-pC.

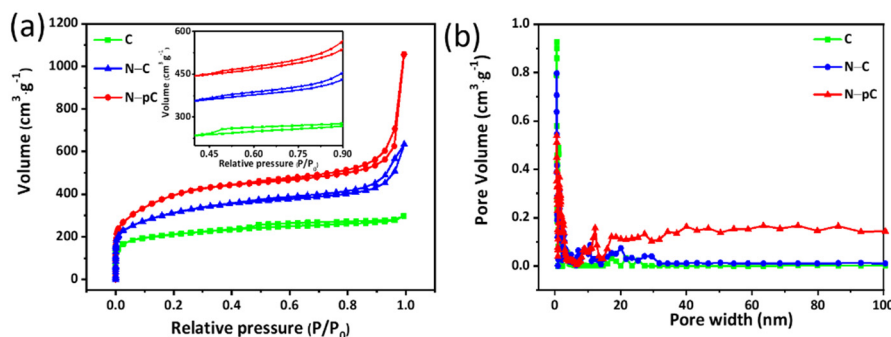


**Figure 3.** (a)  $N_2$  adsorption/desorption isotherms (inset shows the enlarged plots) and (b) the related pore size distribution curves of C, N-C and NpC.

The surface composition of the C, N-C and N-pC samples were investigated by XPS measurements. Figure 4a shows the full spectrum of the three materials. Compared with C, both N-C and N-pC contain N, indicating that the addition of urea can successfully realize N-doping. However, the N content of N-pC (5.18%) is higher than that of N-C (4.65%) due to the existence of NaCl's confining effect acting as a fully sealed nanoreactor, which makes the volatilization and escape of N-containing gas generated by urea pyrolysis reduced. As can be observed from the high-resolution C 1s spectrum of N-pC (Figure 4b), there are four peaks located at 284.67, 285.72, 286.98 and 289.50 eV assigned to the C = C, C = N/C–O, C–N/C = O and O–C = O, respectively [32]. The presence of C = N and C–N bonds suggests that N atoms have been successfully incorporated into the carbon skeleton. Additionally, the N 1s spectra (Figure 4c) can be well separated into four species, corresponding to pyridine N at 398.07 eV, pyrrole N at 399.1 eV, graphitic N at 400.72 eV and oxidized N at 403.4 eV [33]. It has been reported that pyridine N and graphitic N can improve the electrocatalytic ORR performance of the materials, in which pyridine N can promote  $O_2$  adsorption on the neighboring carbon and graphitic N can enhance the electrical conductivity [34–36]. Combining Figure 4a,d, it is easy to find that N-pC possesses a much higher content of pyridine N and graphitic N than N-C. Therefore, the excellent ORR electrocatalytic performance of N-pC will be expected.

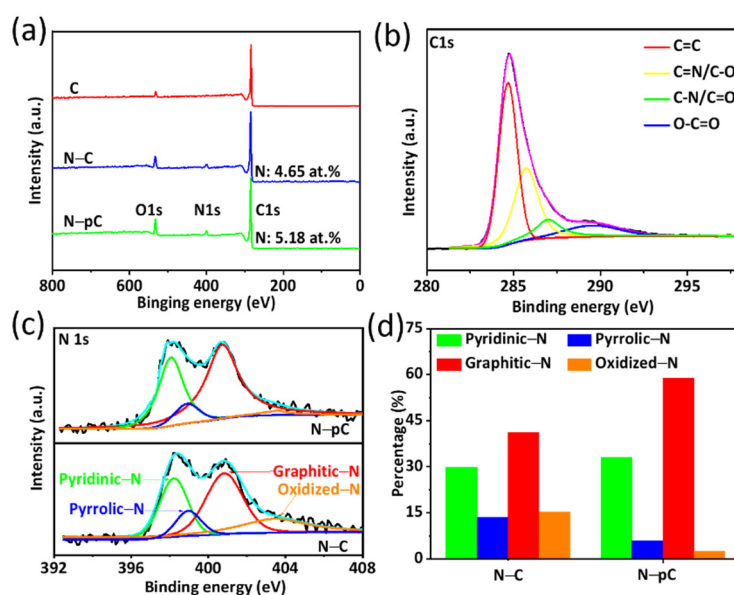


**Figure 4.** (a) XPS spectra of C, N–C and N–pC; (b) C1s high-resolution spectra of N–pC; (c) N1s high-resolution spectra of N–C and N–pC; (d) The percent of different forms of doping nitrogen in N–C and N–pC.

Cyclic voltammetry (CV) was conducted to evaluate the electrocatalytic ORR performance of C, N–C and N–pC in  $O_2$ -saturated 0.1 M KOH electrolyte. As it can be observed from Figure 5a, the CV curves of C, N–C and N–pC show an obvious cathode reduction peak, among which N–pC gives the most positive oxygen reduction peak and the highest peak current density, indicating that N–pC exhibits the highest electrocatalytic activity among the three catalysts. The linear sweep voltammetry (LSV) curves were also measured to further evaluate the ORR activity. As shown in Figure 5b, the C, N–C and commercial Pt/C catalysts have the onset potential ( $E_{onset}$ ) of 0.756 V, 0.913 V and 1.012 V and the half-wave potential ( $E_{1/2}$ ) of 0.585 V, 0.773 V and 0.836 V, respectively. Compared with those catalysts, the N–pC has the more positive onset potential (1.020 V) and half-wave potential (0.863 V) and higher limiting current density. In addition, as presented in Figure 5c, the Tafel slope of N–pC ( $59 \text{ mV dec}^{-1}$ ) is slightly smaller than that of commercial Pt/C ( $62 \text{ mV dec}^{-1}$ ), suggesting that N–pC has a comparable ORR kinetic process to that of commercial Pt/C. All these results suggest that N–pC has better electrocatalytic ORR activity than C, N–C, Pt/C and most of the reported metal-free catalysts (Table S1) in alkaline media. The superior catalytic performance of N–pC can be attributed to the incorporation of highly active N and the 3D hierarchical porous network structure.

To further evaluate the reaction kinetics of the ORR, the polarization curves at different rotation rates of N–pC were acquired (Figure 5d). Based on the corresponding Koutecky–Levich (K–L) plots, the transferred electron number ( $n$ ) of the C catalyst are calculated to be about 2~2.5, suggesting that the ORR on the C electrode follows a two-electron and two-step mechanism. For the N–C catalyst, the  $n$  values are about 3.5, meaning that the ORR current efficiency is widely increased after the N-doping. On the contrary, the values of  $n$  for N–pC are close to 4 in a wide potential range, implying that a  $4e^{-1}$  process occurs on the N–pC electrode (Figure 5e). The RRDE experiments of the C, N–C and N–pC catalysts were carried out to further quantify the  $n$  and  $HO_2^-$  yield. As shown in Figure 5f, the  $n$  values for the C, N–C and N–pC are about 2.4, 3.5 and 4, respectively, entirely consistent with the RDE measurement results. Meanwhile, the  $HO_2^-$  yield at the N–pC is approximately equal to 0 in the investigated potential range, which is much lower than that at N–C and C.

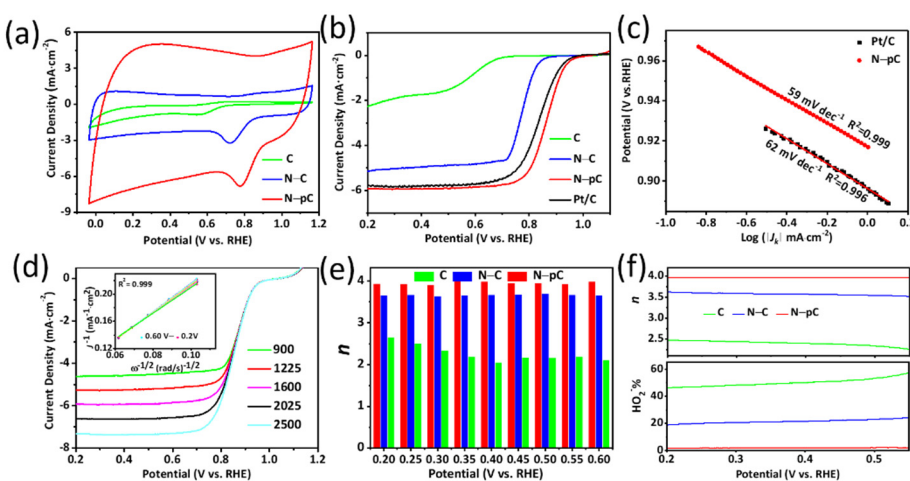


**Figure 5.** (a) CV curves of different catalysts in 0.1 M KOH solutions at a scan rate of  $100 \text{ mV s}^{-1}$ ; (b) LSV curves of different catalysts in 0.1 M KOH solutions at a sweep rate of  $10 \text{ mV s}^{-1}$  and a rotation speed of 1600 rpm; (c) Tafel plots for N-pC and Pt/C; (d) LSV curves of N-pC in 0.1 M KOH recorded at various rotation speeds (900–2500 rpm) at scan rate of  $10 \text{ mV s}^{-1}$  (inset: corresponding K-L plots of N-pC at various potentials); (e) Electron transfer number ( $n$ ) of ORR on N-pC electrode based on RDE test; (f) Electron transfer number ( $n$ ) and corresponding peroxide yield of ORR on N-pC electrode at different potentials based on RRDE test.

In addition, the tolerance for methanol and durability are also important factors in fuel cells. The chronoamperometric response of N-pC and Pt/C catalysts to methanol crossover was tested in the  $\text{O}_2$ -saturated 0.1 M KOH (Figure 6a). After the injection of 1 M methanol, an obvious current attenuation is observed on Pt/C due to methanol oxidation, while there was a negligible change in N-pC, indicating that the N-pC catalyst shows much better tolerance for methanol than commercial Pt/C catalyst. Furthermore, the durability was also evaluated (Figure 6b). After a continuous operation for 16,000 s, the current density on N-pC remains at about 90%, whereas it only maintains 79% on Pt/C under the same condition, confirming that the N-pC catalyst has higher durability than the Pt/C catalyst.

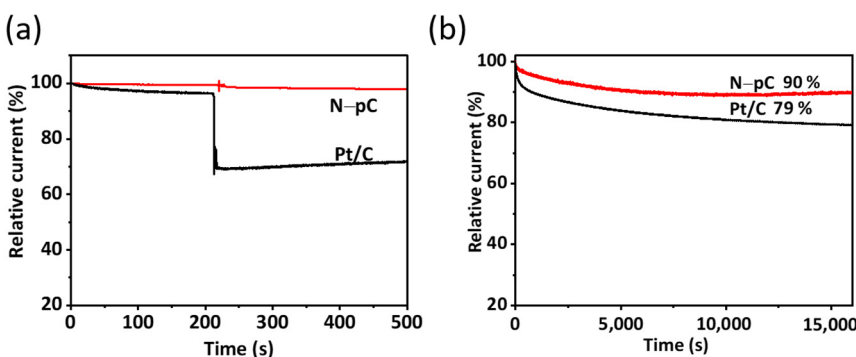


**Figure 6.** Comparison of (a) methanol tolerance and (b) stability for N-pC and 20% Pt/C catalysts measured at  $0.7 \text{ V}$  versus RHE in  $\text{O}_2$ -saturated 0.1 M KOH at a rotation speed of 1600 rpm.

To investigate the potential use of the N-pC catalyst in real batteries, the home-made Zn-air battery (ZAB) was constructed using 6 M KOH solution as the electrolyte, polished pure Zn plate as the anode and N-pC or Pt/C as the air cathode, respectively. The open circuit voltage provided by ZAB using the N-pC catalyst is  $1.50 \text{ V}$  (Figure 7a), higher than that of  $1.43 \text{ V}$  for the commercial Pt/C-based one. The polarization and power density curves of the ZAB were given in Figure 7b. The peak power density of the battery equipped with N-pC catalyst achieves  $223 \text{ mW cm}^{-2}$  at a high current density of  $347.8 \text{ mA cm}^{-2}$ , higher than the Pt/C catalyst ( $182.6 \text{ mW cm}^{-2}$  at  $304.9 \text{ mA cm}^{-2}$ ), suggesting the N-pC

can be employed as a potential cathode electrocatalyst for ZAB. The discharge curves of N-pC-based ZAB at different current densities were measured by typical constant current discharge test. As shown in Figure 7c, the voltage can quickly reach equilibrium when the current changes, confirming that the structure of N-pC is beneficial to the mass-transfer. When the discharge current density recovers to the initial value ( $10 \text{ mA cm}^{-2}$ ) after the high current discharge ( $50 \text{ mA cm}^{-2}$ ), the discharge voltage can be well restored to the initial value, suggesting the good stability of the N-pC. Finally, the ZABs were galvanostatically discharged at  $50 \text{ mA cm}^{-2}$  to investigate their stability and specific capacity. As shown in Figure 7d, the N-pC-based ZAB has higher and more stable voltage than that of the Pt/C-based one during the discharge process. When normalized to the mass of consumed Zn, the specific capacity of the ZAB prepared with N-pC exhibits  $755 \text{ mAh g}^{-1}$ , higher than that of  $709 \text{ mAh g}^{-1}$  for Pt/C and similar or even better than recently reported catalysts (Table S2). All these results suggest that the N-pC catalyst has a good application prospect in ZAB.

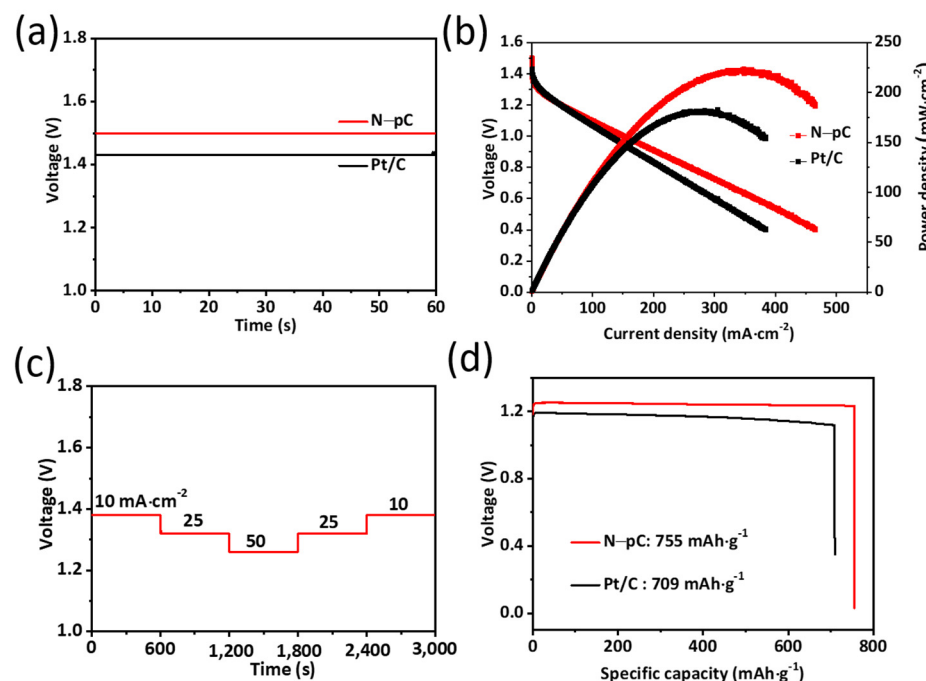


**Figure 7.** (a) Open circuit voltages and (b) discharge polarization curves of N-pC and Pt/C-based batteries; (c) The rate capability behavior of N-pC-based battery; (d) The long-term galvanostatic curves of the Zn-air batteries at  $50 \text{ mA cm}^{-2}$  using N-pC and Pt/C as ORR catalysts.

#### 4. Conclusions

In summary, we successfully prepared a 3D, high-level nitrogen-doped, metal-free (N-pC) electrocatalyst employing urea as a single nitrogen source, NaCl as a fully sealed nanoreactor and gingko shells, constantly renewable and naturally available, as a carbon precursor. Due to the high content of active nitrogen, large surface area ( $1133.8 \text{ m}^2 \text{ g}^{-1}$ ) and 3D hierarchical porous network structure, the N-pC showed a high onset potential of  $1.020 \text{ V}$  and a half-wave potential of  $0.863 \text{ V}$ , and superior tolerance for methanol and stability in alkaline media. Additionally, in ZAB, N-pC showed higher peak power density ( $223 \text{ mW cm}^{-2}$ ), larger specific-capacity ( $755 \text{ mAh g}^{-1}$ ) and better rate-capability than the commercial Pt/C-based ZAB, displaying a good application prospect in metal-air batteries.

**Supplementary Materials:** The following are available online at <https://www.mdpi.com/article/10.3390/pr9122124/s1> Table S1: Comparison of electrocatalytic ORR performance between N-pC and state-of-the-art metal-free catalysts reported in the literatures in alkaline electrolyte; Table

S2: Comparison of the performance of primary Zn-air batteries assembled with various cathodic electrocatalysts.

**Author Contributions:** X.W. and H.Z. designed and carried out the experiment; W.H. and R.L. contributed to the formal analysis and data curation; writing—original draft preparation was mainly accomplished by W.H.; writing—review and editing was implemented by R.L., R.W. and J.S.C. All authors have read and agreed to the published version of the manuscript.

**Funding:** This research was funded by the Education Department of Sichuan Province (Grant 18ZB0494) and Sichuan Science and Technology Program (Grant 2020YJ0299).

**Institutional Review Board Statement:** Not applicable.

**Informed Consent Statement:** Not applicable.

**Conflicts of Interest:** The authors declare no conflict of interest.

## References

- Wang, W.-T.; Batool, N.; Zhang, T.-H.; Liu, J.; Han, X.-F.; Tian, J.-H.; Yang, R. When MOFs meet MXenes: Superior ORR performance in both alkaline and acidic solutions. *J. Mater. Chem. A* **2021**, *9*, 3952–3960. [[CrossRef](#)]
- Cao, F.; Yang, X.; Shen, C.; Li, X.; Wang, J.; Qin, G.W.; Li, S.; Pang, X.; Li, G. Electrospinning synthesis of transition metal alloy nanoparticles encapsulated in nitrogen-doped carbon layers as an advanced bifunctional oxygen electrode. *J. Mater. Chem. A* **2020**, *8*, 7245–7252. [[CrossRef](#)]
- Pan, K.-J.; Hussain, A.M.; Huang, Y.-L.; Gong, Y.; Cohn, G.; Ding, D.; Wachsman, E.D. evolution of solid oxide fuel cells via fast interfacial oxygen crossover. *ACS Appl. Energy Mater.* **2019**, *2*, 4069–4074. [[CrossRef](#)]
- Hong, W.; Feng, X.; Tan, L.; Guo, A.; Lu, B.; Li, J.; Wei, Z. Preparation of monodisperse ferrous nanoparticles embedded in carbon aerogels via in situ solid phase polymerization for electrocatalytic oxygen reduction. *Nanoscale* **2020**, *12*, 15318–15324. [[CrossRef](#)]
- Zhao, L.; Wu, R.; Wang, J.; Li, Z.; Wei, X.; Chen, J.S.; Chen, Y. Synthesis of noble metal-based intermetallic electrocatalysts by space-confined pyrolysis: Recent progress and future perspective. *J. Energy Chem.* **2021**, *60*, 61–74. [[CrossRef](#)]
- Nie, Y.; Li, L.; Wei, Z. Achievements in Pt nanoalloy oxygen reduction reaction catalysts: Strain engineering, stability and atom utilization efficiency. *Chem. Commun.* **2021**. [[CrossRef](#)] [[PubMed](#)]
- Yanhua, L.; Tan, N.; Zhu, Y.; Huo, D.; Zhang, Y.; Sun, S.; Gao, G. Synthesis of porous N-rich carbon/MXene from MXene@Polypyrrole hybrid nanosheets as oxygen reduction reaction electrocatalysts. *J. Electrochem. Soc.* **2020**, *167*, 116503. [[CrossRef](#)]
- Ji, Y.; Dong, H.; Liu, C.; Li, Y. The progress of metal-free catalysts for the oxygen reduction reaction based on theoretical simulations. *J. Mater. Chem. A* **2018**, *6*, 13489–13508. [[CrossRef](#)]
- Zhang, X.; Wang, L. Research progress of carbon nanofiber-based precious-metal-free oxygen reaction catalysts synthesized by electrospinning for Zn-Air batteries. *J. Power Sources* **2021**, *507*, 230280. [[CrossRef](#)]
- Wu, J.; Yang, Z.; Sun, Q.; Li, X.; Strasser, P.; Yang, R. Synthesis and electrocatalytic activity of phosphorus-doped carbon xerogel for oxygen reduction. *Electrochim. Acta* **2014**, *127*, 53–60. [[CrossRef](#)]
- Yokoyama, K.; Sato, Y.; Yamamoto, M.; Nishida, T.; Motomiya, K.; Tohji, K.; Sato, Y. Work function, carrier type, and conductivity of nitrogen-doped single-walled carbon nanotube catalysts prepared by annealing via defluorination and efficient oxygen reduction reaction. *Carbon* **2019**, *142*, 518–527. [[CrossRef](#)]
- Xu, Z.; Zhou, Z.; Li, B.; Wang, G.; Leu, P. Identification of efficient active sites in nitrogen-doped carbon nanotubes for oxygen reduction reaction. *J. Phys. Chem. C* **2020**, *124*, 8689–8696. [[CrossRef](#)]
- Sun, Y.; Wu, J.; Tian, J.; Jin, C.; Yang, R. Sulfur-doped carbon spheres as efficient metal-free electrocatalysts for oxygen reduction reaction. *Electrochim. Acta* **2015**, *178*, 806–812. [[CrossRef](#)]
- Wong, C.H.A.; Sofer, Z.; Klímová, K.; Pumera, M. Microwave exfoliation of graphite oxides in H<sub>2</sub>S plasma for the synthesis of sulfur-doped graphenes as oxygen reduction catalysts. *ACS Appl. Mater. Interfaces* **2016**, *8*, 31849–31855. [[CrossRef](#)] [[PubMed](#)]
- Van, T.T.; Kang, S.G.; Babu, K.F.; Oh, E.-S.; Lee, S.G.; Choi, W.M. Synthesis of B-doped graphene quantum dots as a metal-free electrocatalyst for the oxygen reduction reaction. *J. Mater. Chem. A* **2017**, *5*, 10537–10543.
- Gong, K.; Du, F.; Xia, Z.; Durstock, M.; Dai, L. Nitrogen-doped carbon nanotube arrays with high electrocatalytic activity for oxygen reduction. *Science* **2009**, *323*, 760–764. [[CrossRef](#)]
- Liu, R.; Wu, D.; Feng, X.; Müllen, K. Nitrogen-doped ordered mesoporous graphitic arrays with high electrocatalytic activity for oxygen reduction. *Angew. Chem. Int. Ed.* **2010**, *49*, 2565–2569. [[CrossRef](#)]
- Dai, L.; Xue, Y.; Qu, L.; Choi, H.-J.; Baek, J.-B. Metal-free catalysts for oxygen reduction reaction. *Chem. Rev.* **2015**, *115*, 4823–4892. [[CrossRef](#)]
- Dong, Y.; Yu, M.; Wang, Z.; Zhou, T.; Liu, Y.; Wang, X.; Zhao, Z.; Qiu, J. General synthesis of zeolitic imidazolate frame-work-derived planar-N-doped porous carbon nanosheets for efficient oxygen reduction. *Energy Storage Mater.* **2017**, *7*, 181–188. [[CrossRef](#)]

20. Wang, T.; Chen, Z.-X.; Chen, Y.-G.; Yang, L.-J.; Yang, X.-D.; Ye, J.-Y.; Xia, H.-P.; Zhou, Z.-Y.; Sun, S.-G. Identifying the active site of n-doped graphene for oxygen reduction by selective chemical modification. *ACS Energy Lett.* **2018**, *3*, 986–991. [[CrossRef](#)]
21. Wang, M.; Wu, Z.; Dai, L. Graphitic carbon nitrides supported by nitrogen-doped graphene as efficient metal-free electrocatalysts for oxygen reduction. *J. Electroanal. Chem.* **2015**, *753*, 16–20. [[CrossRef](#)]
22. Ding, W.; Li, L.; Xiong, K.; Wang, Y.; Li, W.; Nie, Y.; Chen, S.; Qi, X.; Wei, Z. Shape fixing via salt recrystallization: A morphology-controlled approach to convert nanostructured polymer to carbon nanomaterial as a highly active catalyst for oxygen reduction reaction. *J. Am. Chem. Soc.* **2015**, *137*, 5414–5420. [[CrossRef](#)]
23. Wang, W.; Luo, J.; Chen, W.; Li, J.; Xing, W.; Chen, S. Synthesis of mesoporous Fe/N/C oxygen reduction catalysts through NaCl crystallite-confined pyrolysis of polyvinylpyrrolidone. *J. Mater. Chem. A* **2016**, *4*, 12768–12773. [[CrossRef](#)]
24. Wang, D.; Xu, H.; Yang, P.; Xiao, L.; Du, L.; Lu, X.; Li, R.; Zhang, J.; An, M. A dual-template strategy to engineer hierarchically porous Fe-N-C electrocatalysts for the high-performance cathodes of Zn-air batteries dagger. *J. Mater. Chem. A* **2021**, *9*, 9761–9770. [[CrossRef](#)]
25. Sa, Y.J.; Seo, D.-J.; Woo, J.; Lim, J.T.; Cheon, J.Y.; Yang, S.Y.; Lee, J.M.; Kang, D.; Shin, T.J.; Shin, H.S.; et al. A general approach to preferential formation of active Fe-N-x sites in Fe-N/C electrocatalysts for efficient oxygen reduction reaction. *J. Am. Chemical Soc.* **2016**, *138*, 15046–15056. [[CrossRef](#)] [[PubMed](#)]
26. Hu, B.-C.; Wu, Z.-Y.; Chu, S.-Q.; Zhu, H.-W.; Liang, H.-W.; Zhang, J.; Yu, S.-H. SiO<sub>2</sub>-protected shell mediated templating synthesis of Fe-N-doped carbon nanofibers and their enhanced oxygen reduction reaction performance. *Energy Environ. Sci.* **2018**, *11*, 2208–2215. [[CrossRef](#)]
27. Meng, F.-L.; Wang, Z.-L.; Zhong, H.-X.; Wang, J.; Yan, J.-M.; Zhang, X.-B. Reactive multifunctional template-induced preparation of Fe-N-doped mesoporous carbon microspheres towards highly efficient electrocatalysts for oxygen reduction. *Adv. Mater.* **2016**, *28*, 7948–7955. [[CrossRef](#)] [[PubMed](#)]
28. Hou, J.; Wen, S.; Chen, J.; Zhao, Q.; Wang, L. Large-scale fabrication of biomass-derived N, S co-doped porous carbon with ultrahigh surface area for oxygen reduction. *Mater. Chem. Phys.* **2021**, *267*, 124601. [[CrossRef](#)]
29. Zhang, J.J.; Sun, Y.; Guo, L.K.; Sun, X.N.; Huang, N.B. Ball-Milling Effect on biomass-derived nanocarbon catalysts for the oxygen reduction reaction. *Chemistry* **2021**, *6*, 6019–6028. [[CrossRef](#)]
30. Borghei, M.; Lehtonen, J.; Liu, L.; Rojas, O.J. Advanced biomass-derived electrocatalysts for the oxygen reduction reaction. *Adv. Mater.* **2018**, *30*, 1703691. [[CrossRef](#)] [[PubMed](#)]
31. Gao, S.; Wei, X.; Fan, H.; Li, L.; Geng, K.; Wang, J. Nitrogen-doped carbon shell structure derived from natural leaves as a potential catalyst for oxygen reduction reaction. *Nano Energy* **2015**, *13*, 518–526. [[CrossRef](#)]
32. Arrigo, R.; Hävecker, M.; Wrabetz, S.; Blume, R.; Lerch, M.; McGregor, J.; Parrott, E.P.J.; Zeitler, J.A.; Gladden, L.F.; Knop-Gericke, A.; et al. tuning the acid/base properties of nanocarbons by functionalization via amination. *J. Am. Chem. Soc.* **2010**, *132*, 9616–9630. [[CrossRef](#)] [[PubMed](#)]
33. Tao, G.; Zhang, L.; Chen, L.; Cui, X.; Hua, Z.; Wang, M.; Wang, J.; Chen, Y.; Shi, J. N-doped hierarchically macro/mesoporous carbon with excellent electrocatalytic activity and durability for oxygen reduction reaction. *Carbon* **2015**, *86*, 108–117. [[CrossRef](#)]
34. Ferre-Vilaplana, A.; Herrero, E. Understanding the chemisorption-based activation mechanism of the oxygen reduction reaction on nitrogen-doped graphitic materials. *Electrochim. Acta* **2016**, *204*, 245–254. [[CrossRef](#)]
35. Guo, D.; Shibuya, R.; Akiba, C.; Saji, S.; Kondo, T.; Nakamura, J. Active sites of nitrogen-doped carbon materials for oxygen reduction reaction clarified using model catalysts. *Science* **2016**, *351*, 361–365. [[CrossRef](#)] [[PubMed](#)]
36. Lai, L.; Potts, J.R.; Zhan, D.; Wang, L.; Poh, C.K.; Tang, C.; Gong, H.; Shen, Z.; Lin, J.; Ruoff, R.S. Exploration of the active center structure of nitrogen-doped graphene-based catalysts for oxygen reduction reaction. *Energy Environ. Sci.* **2012**, *5*, 7936–7942. [[CrossRef](#)]